Inferring earth structure from combined measurements of rotational and translational ground motions

Moritz Bernauer[1], Andreas Fichtner[1], and Heiner Igel[1]

ABSTRACT

We introduce a novel variant of seismic tomography that is based on colocated measurements of rotational and translational ground motions. Our aim is to assess whether rotations may be incorporated successfully into seismic inverse problems to produce better resolved and more realistic tomographic images. Our methodology is based on the definition of apparent S-wave speed as the ratio of rms velocity and rotation amplitudes. The principal advantages of this definition are that (1) no traveltimes measurements are needed and (2) the apparent S-wave speed is independent of source magnitude and source timing. We derive finite-frequency kernels for apparent S-wave speed by using a combination of the adjoint method and ray approximation. The properties of these kernels as a function of frequency bandwidth can be illustrated along with their usefulness for seismic tomography. In multifrequency synthetic inversions, we consider local crosshole tomography and regional-scale earthquake tomography. Our results indicate that S-wave speed variations can be retrieved accurately from colocated rotation and translation measurements, suggesting that our methodology is a promising extension of conventional seismic tomography. Further, apparent S-wave speed can be used to increase vertical resolution in teleseismic tomography for local structures.

INTRODUCTION

Highly resolved tomographic images are essential for a variety of applications, ranging from global-scale geodynamics to local-scale engineering and exploration. There are two general strategies to improve seismic tomography: (1) develop more elaborate modeling and inversion techniques, such as finite-frequency tomography (e.g.,

Yoshizawa and Kennett, 2004) or nonlinear full-waveform inversion (e.g., Fichtner et al., 2008) and (2) incorporate previously unexploited data such as surface-wave amplitudes, exotic phases, and measurements of seismically induced strain (e.g., Mikumo and Aki, 1964) or rotations. In this paper we focus on possible improvements to seismic tomography through incorporating rotation measurements.

Observation of seismically induced rotational ground motions is becoming increasingly feasible and reliable thanks to recent developments of high-precision rotation sensors (e.g., Schreiber et al., 2006, 2009). Several authors report rotations excited by teleseismic waves (e.g., Pancha et al., 2000; Igel et al., 2005, 2007; Cochard et al., 2006). Reports of rotational ground motions recorded in the near-source region can be found in Nigbor (1994), Takeo (1998), Nigbor et al. (2009), Lee et al. (2009), and Wassermann et al. (2009).

Seismically induced rotational ground motions contain information about the structure of the earth. For example, Igel et al. (2005, 2007) and Cochard et al. (2006) infer local phase velocities from colocated measurements of translations and rotations. Wang et al. (2009) and Stupazzini et al. (2009) use the amplitude ratio between transverse motion and rotation rate (vertical axis) to identify low-subsurface velocities associated with sedimentary basin structure. Pham et al. (2009) use rotational signals in the coda of P-waves to constrain crustal scattering. They exploit the fact that rotational motions around the vertical axis are predominantly sensitive to SH motions. Based on full ray-theory modeling, Ferreira and Igel (2009) demonstrate a clearly observable effect of near-receiver heterogeneities on rotational motions of Love waves, suggesting they can be used systematically to infer earth structure.

A first step toward solving structural inverse problems by using measurements of rotational ground motions has been taken by Fichtner and Igel (2009). They study apparent S-wave speed β_a, defined as the ratio of rms translational velocity $\|\mathbf{V}\|_2$ and rms rotation amplitude $\|\omega\|_2$ of a seismic phase or waveform:

$$\beta_a(\mathbf{x}^r) = \frac{\|\mathbf{V}(\mathbf{x}^r)\|_2}{\|\omega(\mathbf{x}^r)\|_2}. \tag{1}$$

Here, $\mathbf{V}(\mathbf{x}^r)$ denotes the displacement velocity at position $\mathbf{x}^r$; ω is the curl of $\mathbf{u}$, i.e., $\omega = \nabla \times \mathbf{u}$; and $\|.\|_2$ is the ℓ_2-norm. Apparent S-wave speed is defined most suitably for windowed portions of a seismogram, where the rms rotation amplitude $\|\omega\|$ is significantly nonzero. We understand that the windowing of translational and rotational recordings is identical. Although Fichtner and Igel (2009) apply windows around body and surface waves, our study focuses on body S-waves only.

Several properties of β_a are particularly interesting in the context of structural inverse problems. First, traveltime measurements are not needed to determine β_a. Second, for a body S-wave in an unbounded and homogeneous medium, β_a is equal to the true S-wave speed, i.e., $\beta_a = \beta$. This suggests that β_a contains directly observable information about earth structure. Third, β_a is independent of source timing and source magnitude — two parameters that often are poorly constrained. Fourth, as demonstrated by Fichtner and Igel (2009), the sensitivity of β_a to true S-wave speed β is largest in the near-receiver region. This contrasts with sensitivities for traveltimes or amplitudes that are nonzero in a volume around the entire raypath (Dahlen et al., 2000; Dahlen and Baig, 2002).

The characteristics of apparent S-wave speed suggest that it can be used for local tomography for active and passive sources. Inferring earth structure from measurements of β_a may complement classical receiver function studies and local earthquake tomography in regions with little or no seismicity. Applications to engineering or exploration problems can be envisioned equally.

In this paper, we explore how apparent S-wave speed β_a may be used to solve structural inverse problems. Our principal objectives are to develop an efficient tool to compute sensitivity kernels for β_a measured on body S-waves and to use them in synthetic inversions for near-receiver structure.

We begin our paper with the theory for computing sensitivity kernels using a combination of the adjoint method and ray approximation. Then, we show sensitivity kernels for β_a measurements in different frequency ranges and compare them to the kernels for measurements of rms velocity and rms rotation. In the synthetic inversions, we focus on applications to local-scale crosshole tomography and regional-scale earthquake tomography.

RAY-THEORETICAL COMPUTATION OF SENSITIVITY KERNELS

Theory

We combine the adjoint method with ray theory to compute sensitivity kernels for β_a. The adjoint method (e.g., Lions, 1968; Tarantola, 1988; Tromp et al., 2005; Fichtner et al., 2006) allows us to avoid the lengthy expressions and approximations of scattering theory used for the same purpose by Yomogida and Aki (1987), Yomogida (1992), Dahlen et al. (2000), and Dahlen and Baig (2002). The resulting formulas can be solved efficiently, and they are correct within the well-known validity range of ray theory (e.g., Červený, 2001). This simplification does not impose restrictions in the context of our study because we focus on the direct S-wave phase and generally consider media with sufficiently smooth heterogeneities.

From the quotient rule applied to the definition of equation 1, we deduce that the relative sensitivity density of β_a with respect to β, denoted by $\beta_a^{-1}\delta_\beta\beta_a = \delta_\beta \ln \beta_a$, can be expressed in terms of the sensitivity densities of $\|\mathbf{V}\|_2$ and $\|\omega\|_2$:

$$\delta_\beta \ln \beta_a = \delta_\beta \ln\|\mathbf{V}\|_2 - \delta_\beta \ln\|\omega\|_2. \quad (2)$$

For notational brevity we omit the dependencies on $\mathbf{x}^r$ wherever possible. The principal result of the adjoint method is that sensitivity densities can be written as time integrals that involve the forward field $\mathbf{u}$ and an adjoint field ψ. In the special case of the sensitivity densities $\delta_\beta \ln \|\mathbf{V}\|_2$ and $\delta_\beta \ln \|\omega\|_2$, we have

$$\delta_\beta \ln\|\mathbf{V}\|_2 = 2\rho\beta^{-1}\int_T \dot{\psi}^V \cdot \mathbf{V} dt \quad (3)$$

and

$$\delta_\beta \ln\|\omega\|_2 = 2\rho\beta^{-1}\int_T \dot{\psi}^\omega \cdot \mathbf{V} dt, \quad (4)$$

where ψ^V and ψ^ω denote the adjoint fields corresponding to measurements of $\|\mathbf{V}\|_2$ and $\|\omega\|_2$, respectively, and where T is the time interval from the source origin time to the end of the observation. The regular velocity field $\mathbf{V}$ is governed by the elastic wave equation:

$$\rho\ddot{\mathbf{u}} - \nabla \cdot (\mathbf{C}:\nabla\mathbf{u}) = \mathbf{f}, \quad (5)$$

where $\mathbf{C}$ and $\mathbf{f}$ denote the fourth-order elastic tensor and an external force density, respectively. The displacement $\mathbf{u}$ and the displacement velocity $\mathbf{V}$ are related through $\mathbf{V} = \dot{\mathbf{u}}$. We omit viscoelastic dissipation because its effect on the shape of sensitivity kernels is negligible. Adjoint fields ψ^V and ψ^ω are determined as the solutions of an adjoint wave equation that is equivalent to the regular wave equation:

$$\rho\ddot{\psi}^V - \nabla \cdot (\mathbf{C}:\nabla\psi^V) = \mathbf{f}^V, \quad \rho\ddot{\psi}^\omega - \nabla \cdot (\mathbf{C}:\nabla\psi^\omega) = \mathbf{f}^\omega. \quad (6)$$

Here, $\mathbf{f}^V$ and $\mathbf{f}^\omega$ are the adjoint sources for ψ^V and ψ^ω, respectively.

In contrast to the initial conditions of the regular wave equation, the adjoint wave equations are complemented by homogeneous terminal conditions. They require that the adjoint field be zero at any time after the end of the observation time span (e.g., Tarantola, 1988). As demonstrated by Fichtner and Igel (2009), the components of $\mathbf{f}^V$ and $\mathbf{f}^\omega$ are given by

$$f_i^V(\mathbf{x},t) = \|\dot{\mathbf{u}}(\mathbf{x}^r)\|_2^{-2}\ddot{u}_i(\mathbf{x}^r,t)\delta(\mathbf{x} - \mathbf{x}^r) \quad (7)$$

and

$$f_i^\omega(\mathbf{x},t) = -\|\omega(\mathbf{x}^r)\|_2^{-2}\varepsilon_{ijk}\omega_k(\mathbf{x}^r,t)\frac{\partial}{\partial x_j}\delta(\mathbf{x} - \mathbf{x}^r), \quad (8)$$

where ε_{ijk} denotes the Levi-Civita alternating symbol. Thus, both adjoint sources act at the receiver location $\mathbf{x}^r$, and their temporal evolution is determined by the observed acceleration and rotation fields. Interestingly, $\mathbf{f}^\omega$ corresponds to an antisymmetric moment tensor source that does not radiate far-field S-waves. This highlights the purely mathematical and abstract nature of the adjoint fields and their sources.

Instead of solving the regular wave equation 5 and adjoint equations 6 numerically, as done by Fichtner and Igel (2009), we use ray-theoretical solutions that are valid in the absence of caustics and strong heterogeneities:

$$\mathbf{u}(\mathbf{x},t) = \mathbf{A}(\mathbf{x})s(t - T_s(\mathbf{x})), \quad (9)$$

$$\psi^V(\mathbf{x},t) = \mathbf{A}^V(\mathbf{x})s^V(T_r(\mathbf{x}) - t), \quad (10)$$

$$\psi^\omega(\mathbf{x},t) = \mathbf{A}^\omega(\mathbf{x})s^\omega(T_r(\mathbf{x}) - t). \qquad (11)$$

The vectors $\mathbf{A}$, $\mathbf{A}^V$, and $\mathbf{A}^\omega$ incorporate the amplitudes and polarizations of the different fields, and the functions s, s^V, and s^ω represent their respective waveforms. The traveltime field T_s is measured from the regular source of the forward field, and the traveltime field T_r is measured from the receiver. Note that the term $(T_r - t)$ appears in the expressions for ψ^V and ψ^ω as a consequence of the terminal conditions. We abstain from a detailed discussion of ray theory because it can be found in standard textbooks (e.g., Červený, 2001; Aki and Richards, 2002).

Combining equations 2–4 and 9–11 yields the following working formula for computing the sensitivity density $\delta_\beta \ln \beta_a$ as a function of position $\mathbf{x}$:

$$\delta_\beta \ln \beta_a(\mathbf{x}) = -2\frac{\rho(\mathbf{x})}{\beta(\mathbf{x})}\mathbf{A}(\mathbf{x})[\mathbf{K}^V(\mathbf{x}) - \mathbf{K}^\omega(\mathbf{x})], \quad (12)$$

with

$$\mathbf{K}^V(\mathbf{x}) = \mathbf{A}^V(\mathbf{x})\int \dot{s}^V(T_r(\mathbf{x}) - t)\dot{s}(t - T_s(\mathbf{x}))dt \qquad (13)$$

and

$$\mathbf{K}^\omega(\mathbf{x}) = \mathbf{A}^\omega(\mathbf{x})\int \dot{s}^\omega(T_r(\mathbf{x}) - t)\dot{s}(t - T_s(\mathbf{x}))dt. \quad (14)$$

Equations 12–14 suggest the following simple recipe for computing the sensitivity kernels $\delta_\beta \ln \beta_a$:

1) Compute the ray-theoretical solution (equation 9) of the regular wavefield $\mathbf{u}$, traveling from the source to the receiver.
2) Use this solution to determine the adjoint sources from equations 7 and 8.
3) Compute the regular wavefield plus the adjoint wavefields (equations 10 and 11) at a point $\mathbf{x}$ in space by solving the ray-tracing and dynamic ray-tracing equations.
4) Assemble the sensitivity kernel according to equations 12–14.

Examples

We illustrate how to compute sensitivity kernels for a medium with a linear velocity gradient from $\beta = 3.2$ km/s at the surface to $\beta = 5.5$ km/s at 350 km depth (Figure 1). The sensitivities of the rms rotation $\delta_\beta \ln\|\omega\|_2$ and the rms velocity $\delta_\beta \ln\|\mathbf{V}\|_2$ exhibit a well-known dependence on the frequency bandwidth of the signal. Comparatively narrow-frequency bands generate broad kernels with sig-
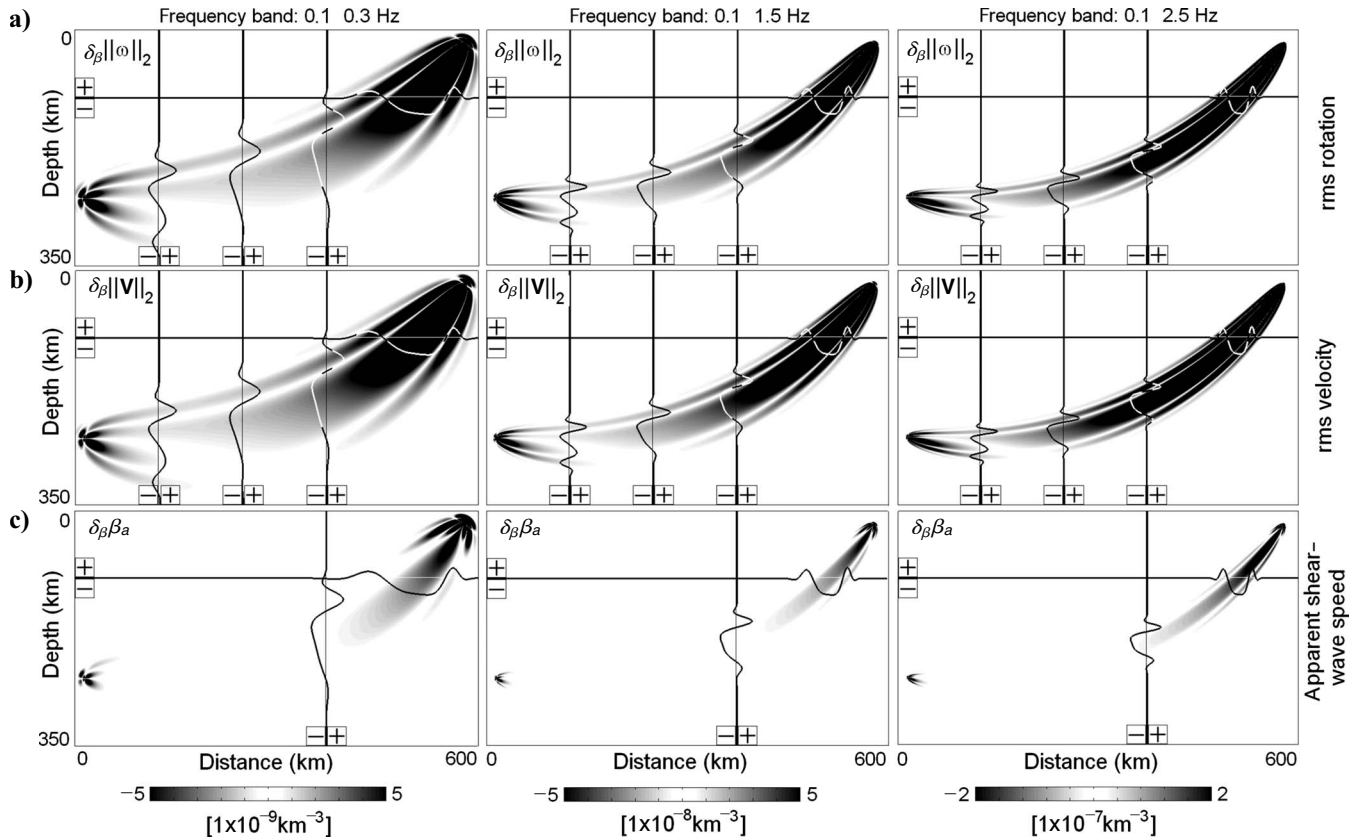

Figure 1. Sensitivity kernels for (a) rms rotation $\|\omega\|_2$, (b) rms velocity $\|\mathbf{V}\|_2$, and (c) apparent S-wave speed β_a. The columns correspond to different frequency bandwidths of the recorded velocity waveform. The superimposed curves are normalized horizontal and vertical cuts through the sensitivity kernels. All sensitivities are with respect to β. The source is at 250-km depth, and the receiver is near the surface.

nificant contributions at larger distances from the geometric raypath. As the bandwidth increases, the kernels become successively narrower and stronger in amplitude.

This effect can be visualized by comparing the three columns of Figure 1, where the frequency bandwidth increases from 0.3 Hz (left column) to 2.5 Hz (right column). Visually, the kernels $\delta_\beta \ln \|\omega\|_2$ and $\delta_\beta \ln \|\mathbf{V}\|_2$ are barely distinguishable. However, their differences become apparent in the kernel for the apparent S-wave speed $\delta_\beta \ln \beta_a$ computed according to equation 2 as the difference $\delta_\beta \ln \beta_a = \delta_\beta \ln \|\mathbf{V}\|_2 - \delta_\beta \ln \|\omega\|_2$.

The β_a kernels in the bottom row of Figure 1 reveal some general characteristics discussed by Fichtner and Igel (2009). The sensitivity decreases with increasing distance from the receiver, the only exception being in the immediate vicinity of the source where all kernels are singular. In the first Fresnel zone, the sensitivity is comparatively small, whereas it remains large in the higher Fresnel zones near the receiver. The regions of high sensitivity of the β_a kernel occupy less space than in the kernels for rotation amplitudes, velocity amplitudes, or finite-frequency traveltimes (Dahlen et al., 2000). This suggests that measurements of β_a can be used to infer small-scale structure, especially in the near-receiver region.

SYNTHETIC INVERSIONS

Here, we give examples of synthetic inversions with β_a measurements by using three scenarios: a local crosshole tomography, a regional earthquake tomography, and a comparison of inversions with rms amplitudes and β_a measurements. These examples illustrate the potential range of application and possible advantages of our approach. To obtain optimal results, we use a nonlinear optimization scheme with successively increasing frequency bandwidth.

We denote by $\beta_{a,i}^0$ and $\beta_{a,i}$ the apparent S-wave speeds for the reference S-wave model $\beta^0(\mathbf{x})$ and the perturbed model $\beta^0(\mathbf{x}) + \delta\beta(\mathbf{x})$. The subscript i refers to different source and receiver locations, different frequencies, or combinations of them. For simplicity, we refer to $\beta_{a,i}$ and $\beta_{a,i}^0$ as data and synthetics, respectively, keeping in mind that the following examples are synthetic inversions.

We want to recover the perturbation $\delta\mathbf{m}$ through the minimization of the least-squares misfit functional:

$$E = \frac{1}{2}\sum_{i=1}^{n}(\beta_{a,i} - \beta_{a,i}^0)^2. \quad (15)$$

The earth model is parameterized by a set of N basis functions, $h_k(\mathbf{x})$, $k = 1,\ldots,N$, that allow us to express the S-wave speed model $\beta(\mathbf{x})$ as $\beta(\mathbf{x}) = \Sigma_{k=1}^{N}\beta_k h_k(\mathbf{x})$, where the values of β_k are scalars. For simplicity, we choose the basis functions to be cubic blocks. The derivative of the objective function E with respect to the coefficient β_k is now given by the projection of the sensitivity kernel $\delta_\beta\beta_{a,i}(\mathbf{x})$ onto the basis function h_k:

$$\frac{\partial E}{\partial \beta_k} = \sum_{i=1}^{n}(\beta_{a,i} - \beta_{a,i}^0)\int_G h_k(\mathbf{x})\delta_\beta\beta_{a,i}(\mathbf{x})d^3\mathbf{x},$$
$$k = 1,\ldots,N. \quad (16)$$

Here, G denotes the volume of the earth model. For multiple source and receiver geometries, the total gradient is equal to the weighted sum of the single-source and single-receiver gradients, where the weights are the residuals $\beta_{a,i} - \beta_{a,i}^0$.

Using the derivative E, we minimize the misfit iteratively with a preconditioned steepest-descent algorithm. The preconditioner is a Gaussian taper that eliminates the singularity of the sensitivity kernels directly at the receiver. It thus prevents the minimization scheme from converging toward a local minimum where all heterogeneities are concentrated at receiver locations. During the iterative misfit minimization, we successively increase the frequency content. This allows us to ensure the quasi-linearity of the misfit functional with respect to earth model perturbations.

Scenario I: Local-scale crosshole tomography

Crosshole tomography is a standard tool used to image small-scale structures for engineering and exploration applications (e.g., Wong, 2000; Angioni et al., 2003) and in studies of local tectonics (Bleibinhaus et al., 2007). In our first example (Figure 2a), we consider two 80-m-deep boreholes separated by 80 m. Eight seismic sources at depths of 5–75 m generate S-waveforms recorded at 70 equally spaced receivers at depths between 5 and 75 m. During the iteration, we successively use the following frequency bands: 0.1–0.6, 0.1–0.9, 0.1–1.2, 0.1–1.5, and 0.1–1.8 kHz.

The target model that we want to invert for consists of two high-velocity perturbations and a low-velocity perturbation superimposed on a homogeneous background S-wave velocity of 2 km/s. The perturbations represent strong changes of the medium properties in the shallow subsurface. To comply with the requirements of ray theory, used to compute waveforms and sensitivity kernels, we choose the perturbations to be smooth. They have similar complexity to synthetic structures chosen by various authors (e.g., Linde et al., 2008; Zhou et al., 2008).

The fictitious data set used for the synthetic tomography contains 40 recording sets (eight sources, five frequencies), a collection of which is shown in Figure 3. Although the complexity of the sensitivity kernels dictates a cautious interpretation of β_a in terms of earth structure, the strength of β_a variations is proportional to the frequency bandwidth. Moreover, data produced by sources close to the perturbations (Figure 3c) give a hint to changes between high- and low-velocity zones as well as to the perturbation intensities.

The inversion starts with a misfit minimization for a homogeneous initial model and the narrowest frequency band (0.1–0.6
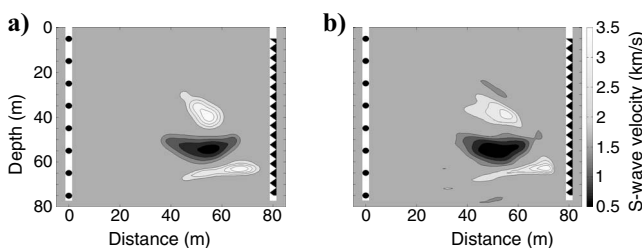

Figure 2. Scenario I crosshole tomography. (a) Original S-wave velocity model: two 80-m-deep boreholes (vertical white columns) separated by 80 m. Sources and receivers are spaced equally at depths between 5 and 75 m. The right borehole contains 70 receivers (black sawtooth line) that record signals from eight sources (black bullets) in the left borehole. The synthetic model contains low- and high-speed variations on a constant S-wave velocity background of 2 km/s. (b) Final model after inversion over successively broader frequency bands. The original model of (a) is reproduced well.

kHz). After seven iterations, the synthetics reproduce the observations well (Figure 4). The resulting image can be used as the initial model for the inversion in the next (higher) frequency band. We repeat this procedure until we reach the fifth frequency band (0.1–1.8 kHz). The final model is presented in Figure 2b.

The final inversion localizes low- and high-velocity zones correctly. The shapes and intensities of the perturbations are similar to the original model. Small differences in the shape of the perturbations remain, as is routine in tomographic models. They may be attributed to imperfect data coverage. We note that this example provides proof of concept; it does not represent a systematic resolutions study of the type that would be needed for specific engineering or exploration applications.

Scenario II: Regional-scale earthquake tomography

The second example shows that our method is well suited to regional-scale tomography problems. Here, we mimic a regional earthquake tomography study across a subduction zone as performed, for example, in the southern Andes by Bohm et al. (2002) and in Central America by Syracuse et al. (2008). Inferring structural heterogeneity in tectonically active zones is essential in studies of earth dynamics (e.g., Schuberth et al., 2009). The target model, shown in Figure 5a, contains a −1-km/s low-velocity region that represents a zone of subduction-related melt ascent. This region is flanked by two +1-km/s high-velocity regions. The background velocity is 4.5 km/s.

The seismic experiment includes six earthquake sources, regularly spaced along a fictitious downgoing plate at depths between 80 and 200 km. Some 120 receiver stations are spaced equally in a 238-km-long surface profile. The frequency bands for the inversion are 0.1–1.0, 0.1–1.5, and 0.1–2.0 Hz. They provide a data set of 18 recording sets (six sources, three frequencies). In Figure 6, data curves are plotted for all frequency bands and sources at the profile locations $x = 100$ km, $x = 180$ km, and $x = 260$ km. Our ad hoc interpretation of data plots is restricted to the same level as for scenario I, and the inversion principle is analogous to that used in scenario I.

Figure 7 shows the minimization of the data misfit between data and synthetics for the narrowest frequency band over nine iteration steps. The inversion result (Figure 5b) reproduces the main characteristics of the subduction zone model well. Nevertheless, there are some artifacts, especially in source regions. These may be a consequence of the singularity of the β_a kernels directly at the source locations.

Scenario III: Comparative example

Measurements of apparent S-wave speeds are advantageous in tomographic problems where the particular shape of their sensitivity kernels can be exploited. This is the case, for example, in teleseismic

tomography for local structures where all incident rays are nearly vertical. Using observation data with sensitivities that extend from the source to the receiver (e.g., rms amplitudes or arrival times) may lead to considerable vertical smearing. This can be avoided by using observation data that are sensitive primarily to near-receiver structures, such as apparent S-wave speed.

The synthetic inversion summarized in Figure 8 illustrates this effect. The input structure (Figure 8a) contains a fictitious asthenos-
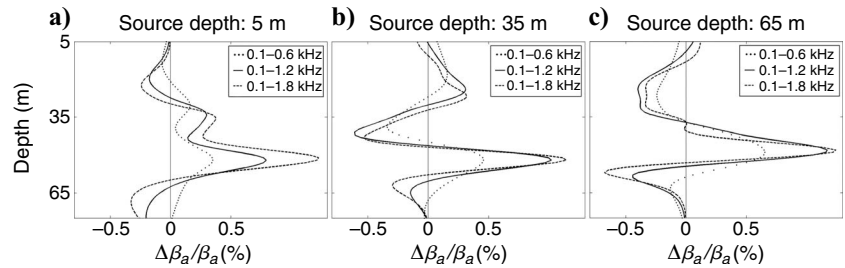

Figure 3. Relative variations of apparent S-wave speed $\Delta\beta_a/\beta_a$ for seismic sources at depths of (a) 5, (b) 35, and (c) 65 m for frequency bands of 0.1–0.6, 0.1–1.2, and 0.1–1.8 kHz.
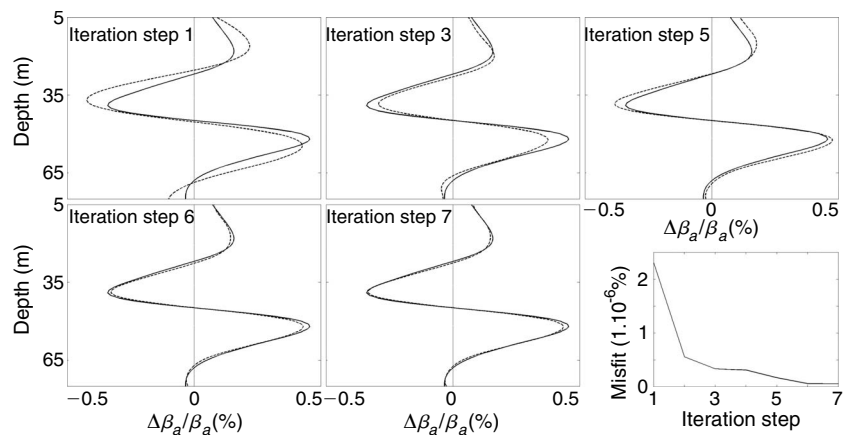

Figure 4. Misfit optimization between observed data (solid curves) and synthetic data (broken curves) for seven iteration steps applied to the data set produced by a source at 5-m depth and a frequency band 0.1–0.6 kHz. Data and synthetics match well after seven iterations.
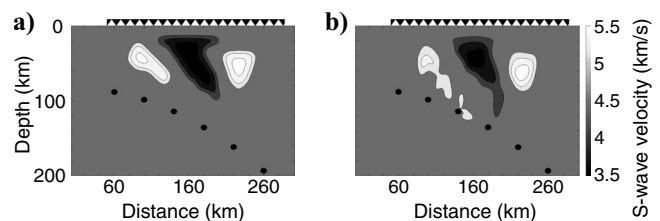

Figure 5. Scenario II modeling of a typical subduction zone with a low-speed region caused by melting processes and two adjoining high-speed zones. (a) Original S-wave velocity model with six earthquake sources (black bullets) regularly spaced along the downgoing plate at depths between 80 and 200 km. The black triangles represent a surface-receiver profile of 120 recording stations. (b) Inversion model including six sources, 120 receivers, and three frequency bands. The inversion results show that the approach combining translational and rotational measurements is effective for regional-scale tomography.

pheric low-velocity layer below 100 km depth as well as other heterogeneities. We use 21 equally spaced receivers, four sources at around 250-km depth, and the same inversion scheme as in the previous two scenarios. If only rms amplitudes are used, the low-velocity layer smears into shallow depths above 100 km (Figure 8b). A similar result would be expected for traveltime tomography because amplitude and traveltime kernels are similar geometrically. The apparent S-wave speed, however, provides an accurate image of the

upper 100 km, with negligible vertical smearing. Structures below 100 km depth cannot be recovered by using rms amplitudes or apparent S-wave speed.

DISCUSSION

Our novel variant of seismic tomography is based on colocated measurements of translational and rotational ground motions. For the iterative solution of the inverse problem, we combine the adjoint method and ray approximation. Our use of ray theory was motivated by its low computational cost, which allows us to perform many numerical experiments and thus gain an intuitive understanding of inverse problems that involve measurements of apparent S-wave speed. Although numerically efficient, the limitations of ray theory restricted this study to smooth models and high-frequency S-waves. This limitation may be mitigated in future applications by using full numerical wave-propagation schemes that allow us to include lower frequencies and any type of seismic wave.

The measurement of the apparent S-wave speed is attractive because it is independent of source timing and source magnitude. This property simplifies the combined source-structure inverse problem. Moreover, no arrival-time measurements are needed. In principle, fully numerical wave propagation allows us to use any part of a seismogram to measure apparent S-wave speed (Fichtner and Igel, 2009).

A disadvantage of our method lies in the difficulty of measuring the amplitudes of translational and rotational ground motions with high precision. Although the synthetic inversions presented here clearly show that apparent S-wave speed measurements result in well-resolved tomographic images, variations of apparent S-wave speed induced by unknown earth structures may be difficult to identify. We are working on a detailed analysis of variations of apparent S-wave speed.
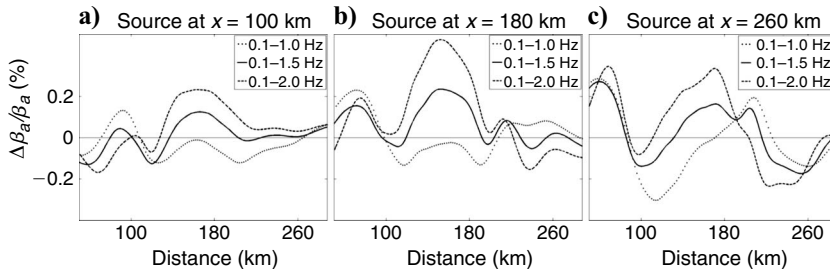

Figure 6. Relative variations of the apparent S-wave speed $\Delta\beta_a/\beta_a$ for different earthquake source locations: (a) $x = 100$ km, depth $= 96$ km; (b) $x = 180$ km, depth $= 134$ km; and (c) $x = 260$ km, depth $= 192$ km. Data are shown for frequency bands $0.1-1.0$, $0.1-1.5$, and $0.1-2.0$ Hz.
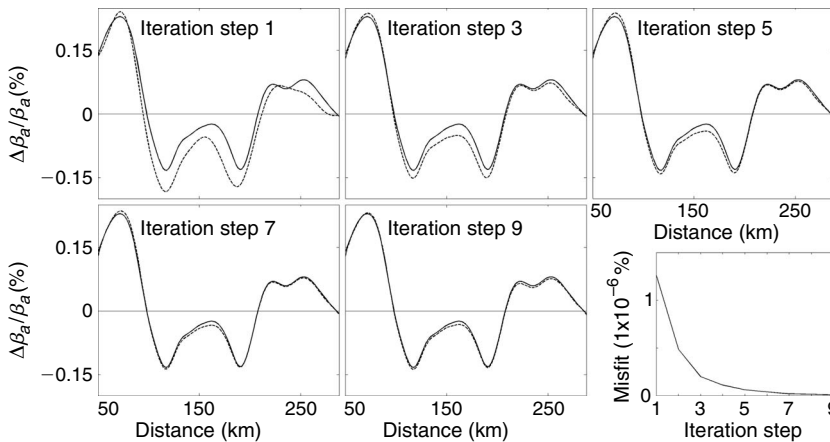

Figure 7. Misfit optimization between observed data (solid curves) and synthetic data (broken curves) for an earthquake source at $x = 180$ km, depth $= 134$ km, and the frequency band $0.1-1.0$ Hz. After nine iterations, data and synthetics match well.

CONCLUSIONS

The principal objective of this study was to assess whether measurements of seismically induced rotational ground motions can be incorporated successfully into seismic inverse problems to yield better resolved and more realistic tomographic images. From the synthetic tests presented in the previous sections we conclude that collocated displacement and rotation measurements, combined to the apparent S-wave speed, suggest a promising extension of conventional seismic tomography.

Some necessary steps to develop this methodology further are (1) extracting structural information from real measurements of apparent S-wave speed, (2) transitioning from ray theory
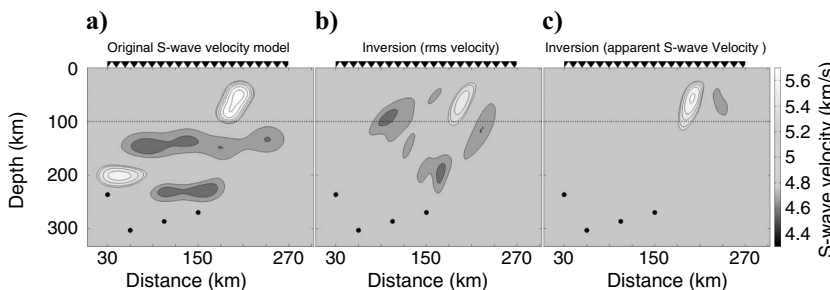

Figure 8. Scenario III. Comparison of inversions using rms amplitude and apparent S-wave speed. (a) Original earth model. Inversion results using (b) rms amplitude only and (c) apparent S-wave speed.

to fully numerical wave propagation, (3) incorporating additional seismic phases and surface waves, (4) performing systematic resolution analyses, and (5) comparing our method with standard tomographic methods. Further application of the proposed method is dependent on the availability of more rotational ground-motion data and on development and improvement of sensor technologies that, unlike currently available ring lasers, are portable.

ACKNOWLEDGMENTS

REFERENCES

Aki, K., and P. G. Richards, 2002, Quantitative seismology, 2nd ed.: University Science Books.

Angioni, T., R. D. Rechtien, S. J. Cardimona, and R. Luna, 2003, Crosshole seismic tomography and borehole logging for engineering site characterization in Sikeston, MO, USA: Tectonophysics, **368**, 119–137.

Bleibinhaus, F., J. A. Hole, T. Ryberg, and G. S. Fuis, 2007, Structure of the California Coast Ranges and San Andreas fault at SAFOD from seismic waveform inversion and reflection imaging: Journal of Geophysical Research, **112**, B06315.

Bohm, M., S. Lüth, H. Echtler, G. Asch, K. Bataille, C. Bruhn, A. Rietbrock, and P. Wigger, 2002, The southern Andes between 36° and 40° latitude: Seismicity and average seismic velocities: Tectonophysics, **356**, 275–289.

Červený, V., 2001, Seismic ray theory: Cambridge University Press.

Cochard, A., H. Igel, B. Schuberth, W. Suryanto, A. Velikoseltsev, U. Schreiber, J. Wassermann, F. Scherbaum, and D. Vollmer, 2006, Rotational motions in seismology: Theory, observation, simulation, in R. Teisseyre, M. Takeo, and E. Majewski, eds., Earthquake source asymmetry, structural media and rotation effects: Springer Verlag, 391–411.

Dahlen, F. A., and A. M. Baig, 2002, Fréchet kernels for body-wave amplitudes: Geophysical Journal International, **150**, 440–466.

Dahlen, F. A., S.-H. Hung, and G. Nolet, 2000, Fréchet kernels for finite-frequency travel times — I. Theory: Geophysical Journal International, **141**, 157–174.

Ferreira, A. M. G., and H. Igel, 2009, Rotational motions of seismic surface waves in a laterally heterogeneous earth: Bulletin of the Seismological Society of America, **99**, 1429–1436.

Fichtner, A., H.-P. Bunge, and H. Igel, 2006, The adjoint method in seismology: I. — Theory: Physics of the Earth and Planetary Interiors, **157**, 86–104.

Fichtner, A., and H. Igel, 2009, Sensitivity densities for rotational ground motion measurements: Bulletin of the Seismological Society of America, **99**, 1302–1314.

Fichtner, A., B. L. N. Kennett, H. Igel, and H.-P. Bunge, 2008, Theoretical background for continental and global scale full-waveform inversion in the time-frequency domain: Geophysical Journal International, **175**, 665–685.

Igel, H., A. Cochard, J. Wassermann, A. Flaws, U. Schreiber, A. Velikoseltsev, and N. P. Dinh, 2007, Broad-band observations of earthquake-induced rotational ground motions: Geophysical Journal International, **168**, 182–197.

Igel, H., U. Schreiber, A. Flaws, B. Schuberth, A. Velikoseltsev, and A. Cochard, 2005, Rotational motions induced by the M 8.1 Tokachi-oki earthquake, September, 25, 2003: Geophysical Research Letters, **32**, L08309.

Lee, W. H. K., B. S. Huang, C. A. Langston, C. J. Lin, C. C. Liu, T. C. Shin, T. L. Teng, and C. F. Wu, 2009, Review: Progress in rotational ground-motion observations from explosions and local earthquakes in Taiwan: Bulletin of the Seismological Society of America, **99**, 958–967.

Linde, N., A. Tryggvason, J. E. Peterson, and S. S. Hubbard, 2008, Joint inversion of crosshole radar and seismic traveltimes acquired at the South Oyster bacterial transport site: Geophysics, **73**, no. 4, G29–G37.

Lions, J. L., 1968, Contrôle optimal de systèmes gouvernés par des équations aux dérivées partielles: Dunod Gauthier-Villars.

Mikumo, T., and K. Aki, 1964, Determination of local phase velocity by intercomparison of seismograms from strain and pendulum instruments: Journal of Geophysical Research, **69**, 721–731.

Nigbor, R. L., 1994, Six-degree-of-freedom ground motion measurement: Bulletin of the Seismological Society of America, **84**, 1665–1669.

Nigbor, R. L., J. R. Evans, and C. R. Hutt, 2009, Laboratory and field testing of commercial rotational seismometers: Bulletin of the Seismological Society of America, **99**, 1215–1227.

Pancha, A., T. H. Webb, G. E. Stedman, D. P. McLeod, and K. U. Schreiber, 2000, Ring laser detection of rotations from teleseismic waves: Geophysical Research Letters, **27**, 3553–3556.

Pham, N. D., H. Igel, J. Wassermann, M. Käser, J. de la Puente, and U. Schreiber, 2009, Observations and modeling of rotational signals in the P-coda: Constraints on crustal scattering: Bulletin of the Seismological Society of America, **99**, 1315–1332.

Schreiber, K. U., J. N. Hautmann, A. Velikoseltsev, J. Wassermann, H. Igel, J. Otero, F. Vernon, and J.-P. R. Wells, 2009, Ring laser measurements of ground rotation for seismology: Bulletin of the Seismological Society of America, **99**, 1190–1198.

Schreiber, U., G. E. Stedman, H. Igel, and A. Flaws, 2006, Ring laser gyroscopes as rotation sensors for seismic wave studies, in R. Teisseyre, M. Takeo, and E. Majewski, eds., Earthquake source asymmetry, structural media and rotation effects: Springer Verlag, 377–387.

Schuberth, B., H.-P. Bunge, G. Steinle-Neumann, C. Moder, and J. Oeser, 2009, Thermal versus elastic heterogeneity in high-resolution mantle circulation models with pyrolite composition: High plume excess temperatures in the lowermost mantle: Geochemistry Geophysics Geosystems, **10**, Q01W01.

Stupazzini, M., J. de la Puente, C. Smerzini, M. Käser, H. Igel, and A. Castellani, 2009, Study of rotational ground motion in the near-field region: Bulletin of the Seismological Society of America, **99**, 1271–1286.

Syracuse, E. M., G. A. Abers, K. Fischer, L. Mackenzie, C. Rychert, M. Protti, V. Gonzáles, and W. Strauch, 2008, Seismic tomography and earthquake locations in the Nicaraguan and Costa Rican upper mantle: Geochemistry Geophysics Geosystems, **9**, Q07S08.

Takeo, M., 1998, Ground rotational motions recorded in near-source region of earthquakes: Geophysical Research Letters, **25**, 789–792.

Tarantola, A., 1988, Theoretical background for the inversion of seismic waveforms, including elasticity and attenuation: Pure and Applied Geophysics, **128**, 365–399.

Tromp, J., C. Tape, and Q. Liu, 2005, Seismic tomography, adjoint methods, time reversal and banana-doughnut kernels: Geophysical Journal International, **160**, 195–216.

Wang, H., H. Igel, F. Gallovic, and A. Cochard, 2009, Source and basin effects on rotational ground motions: Comparison with translations: Bulletin of the Seismological Society of America, **99**, 1162–1173.

Wassermann, J., S. Lehndorfer, H. Igel, and U. Schreiber, 2009, Performance test of a commercial rotational motion sensor: Bulletin of the Seismological Society of America, **99**, 1449–1456.

Wong, J., 2000, Crosshole seismic imaging for sulfide orebody delineation near Sudbury, Ontario, Canada: Geophysics, **65**, 1900–1907.

Yomogida, K., 1992, Fresnel zone inversion for lateral heterogeneities in the earth: Pure and Applied Geophysics, **138**, 391–406.

Yomogida, K., and K. Aki, 1987, Amplitude and phase data inversions for phase velocity anomalies in the Pacific Ocean basin: Geophysical Journal, **88**, 161–204.

Yoshizawa, K., and B. L. N. Kennett, 2004, Multimode surface wave tomography for the Australian region using a three-stage approach incorporating finite frequency effects: Journal of Geophysical Research, **109**, doi: 10.1029/2002JB002254.

Zhou, B., S. Greenhalgh, and A. Green, 2008, Nonlinear traveltime inversion scheme for crosshole seismic tomography in tilted transversely isotropic media: Geophysics, **73**, no. 4, D17–D33.